SANDIA REPORT
SAND2021-11561
Printed September 2021

Sandia National Laboratories

Source Physics Experiment: Rock Valley Interferometric Synthetic Aperture RADAR Earthquake Detection Study

David A. Yocky

Prepared by
Sandia National Laboratories
Albuquerque, New Mexico
87185 and Livermore,
California 94550

Issued by Sandia National Laboratories, operated for the United States Department of Energy by National Technology & Engineering Solutions of Sandia, LLC.

NOTICE: This report was prepared as an account of work sponsored by an agency of the United States Government. Neither the United States Government, nor any agency thereof, nor any of their employees, nor any of their contractors, subcontractors, or their employees, make any warranty, express or implied, or assume any legal liability or responsibility for the accuracy, completeness, or usefulness of any information, apparatus, product, or process disclosed, or represent that its use would not infringe privately owned rights. Reference herein to any specific commercial product, process, or service by trade name, trademark, manufacturer, or otherwise, does not necessarily constitute or imply its endorsement, recommendation, or favoring by the United States Government, any agency thereof, or any of their contractors or subcontractors. The views and opinions expressed herein do not necessarily state or reflect those of the United States Government, any agency thereof, or any of their contractors.

Printed in the United States of America. This report has been reproduced directly from the best available copy.

Available to DOE and DOE contractors from
U.S. Department of Energy
Office of Scientific and Technical Information
P.O. Box 62
Oak Ridge, TN 37831

Telephone: (865) 576-8401
Facsimile: (865) 576-5728
E-Mail: reports@osti.gov
Online ordering: http://www.osti.gov/scitech

Available to the public from
U.S. Department of Commerce
National Technical Information Service
5301 Shawnee Rd
Alexandria, VA 22312

Telephone: (800) 553-6847
Facsimile: (703) 605-6900
E-Mail: orders@ntis.gov
Online order: https://classic.ntis.gov/help/order-methods/

ABSTRACT

Seismic signals from 1993 show a series of magnitude (Mw) 3.7 or less seismic events in Rock Valley on the Nevada National Security Site (NNSS). Historic synthetic aperture radar images of that location were found that could provide interferometric synthetic aperture radar (InSAR) measures of the ground height during 1993. Given this historic SAR imagery, we explore answering the question if ground movement from the 1993 Rock Valley earthquake activity could be sensed by remote sensing means. Finding earthquake surface movement would assist in locating the Rock Valley fault and the 1993 earthquake hypocenter where the Source Physics Experiment Phase III series of experiments will be conducted.

In this report, we show that InSAR can sense very small height differences, and for the European Radar Satellite-1 InSAR collections during 1992 and 1993 over Rock Valley earth surface movements were measured with 8 mm uplift and 12.5 mm subsidence over isolated areas. One of these earth movement areas coincides with an InSAR image pair coherence drop between March 5, 1993 and June 18, 1993. The coherence drop is over an approximately 13 square km area south southeast of Skull Mountain centered at 36^{o} 43' 30" N latitude and 116^{o} 05' 00" W longitude.

Measured small surface movement and a loss of InSAR coherence may be caused by the series of earthquakes. The location of these InSAR detections may also coincide with water drainage or erosion displacement. There are no records to disambiguate the earthquake and erosion earth surface motion possibilities. Therefore, the InSAR findings of earth surface movement by InSAR are inconclusive.

ACKNOWLEDGEMENTS

The Source Physics Experiments (SPE) would not have been possible without the support of many people from several organizations. The author wishes to express his gratitude to the National Nuclear Security Administration, Defense Nuclear Nonproliferation Research and Development, and the SPE working group, a multi-institutional and interdisciplinary group of scientists and engineers.

Sandia National Laboratories is a multimission laboratory managed and operated by National Technology and Engineering Solutions of Sandia LLC, a wholly owned subsidiary of Honeywell International Inc. for the U.S. Department of Energy's National Nuclear Security Administration under contract DE-NA0003525. SAND 2021-####.

CONTENTS

LIST OF FIGURES

LIST OF TABLES

This page left blank

ACRONYMS AND DEFINITIONS

Abbreviation	Definition
DEM	Digital elevation model
DInSAR	Differential interferometric synthetic aperture radar
ERS-1	European RADAR Satellite -1
GHz	Giga-Hertz
InSAR	Interferometric synthetic aperture radar
Mw	Moment magnitude
NNSS	Nevada National Security Site
RADAR	Radio detection and ranging
RGB	Red green blue
RMS	Root mean square
SAR	Synthetic aperture radar
SBAS	Small baseline subset
SNR	Signal-to-noise ratio
SVD	Singular value decomposition

1. INTRODUCTION

Source Physics Experiment is planning Phase III of the experiment series. For this case, the explosion tests will be close to a past earthquake epicenter. In 1993, a sequence of unusual and very shallow earthquakes in Area 27 of the Nevada National Security Site (NNSS) at Rock Valley occurred. By setting off an explosion at the hypocenter of a prior Rock Valley earthquake and recording the seismic signals at sites where the original earthquake was recorded, the two sources can be directly compared. Therefore, the hypocenter of the target earthquake needs to be well known.

Differential interferometric synthetic aperture radar (DInSAR) techniques have been developed over the years to successfully generate large-scale surface deformation maps [1]. This approach has been applied to the analysis of a single deformation episode such as earthquakes [2], [3], [4]. Published detected earth deformation resulting from earthquakes have detected earthquakes with magnitudes (Mw) of 4.7 or greater using DInSAR methods [5].

The lower limit of earthquake earth deformation detection using DInSAR is not uniform because of geology, surface height gradients, and surface composition differences around the world. However, the accuracy of DInSAR type measurements from earth-orbiting synthetic aperture radar (SAR) have been determined to be between 3 mm to 1 cm for diffuse targets [1]. Therefore, the question if DInSAR or another interferometric SAR (InSAR) technique can detect surface deformation from a given earthquake depends on if deformation exceeds the above sensitivity limitations.

If the Rock Valley earthquake sequence created surface movements, InSAR techniques might detect this and locate where surface deformation occurred if the movement was great enough. Therefore, InSAR surface movement of Rock Valley was explored using satellite SAR imagery collected in 1992 and 1993.

2. SAR IMAGERY

It was discovered the European Radar Satellite-1 (ERS-1), which operationally orbited Earth from 1991 – 2000, captured coherent, possibly interferometrically-compatible, imagery over NNSS, Rock Valley from April 12, 1992 to November 24, 1993. During this period, 11 complex-valued (magnitude and phase) images were collected and documented in Table 2-1. ERS-1 was a C-Band (5.3 GHz) SAR with a 5.6 cm wavelength. An image footprint was 100 km on a side with 26 m range resolution. Square pixel images were then 26 m resolution on a side.

Repeat-collection geometry determines the coherence between image pairs. If the image pairs are incoherent, interferometric processing is not viable. Each image pair geometry must be examined. For example, in Table 2-1, image 3 is coherent with image 4. Likewise, image 4 is coherent with image 5. But image 3 is not coherent with image 5. Image 3 and image 5 are not coherent because the difference in collection geometry is too great. This geometry difference is captured by the interferometric baseline. This InSAR measure and other interferometric processing will be defined and discussed in the next section.

Table 2-1: A list of ERS-1 images and coherent pairs

Date	Image	Coherent with	Note
April 12, 1992	1	None	Baselines > 1 km
September 9, 1992	2	None	Baselines > 1 km
December 25, 1992	3	4	
January 29, 1993	4	3,5,7,8,9,10	
March 3, 1993	5	4,7,8,9	
April 9, 1993	6	None	Baselines > 1 km
June 18, 1993	7	4,5,8,9	
July 23, 1993	8	4,5,7	
August 27, 1993	9	4,5,7	
October 1, 1993	10	4	
November 23, 1993	11	None	Baselines > 1 km

2.1. SAR Interferometry

For SAR imaging, coherence between two images is a function of time, of system noise, and of spatial correspondence.

$$|\gamma| = |\gamma_t| \cdot |\gamma_{snr}| \cdot |\gamma_s| \tag{1}$$

where

$|\gamma_t|$ is the time-dependent coherence,

$|\gamma_{snr}|$ is the signal-to-noise (SNR) coherence.

The spatial coherence, γ_s, can be broken into two components: image-to-image registration and collection geometry difference or

$$|\gamma_s| = |\gamma_r| \cdot |\gamma_g| \tag{2}$$

where

$|\gamma_r|$ is the registration coherence,

$|\gamma_g|$ is the geometry-dependent coherence.

The temporal coherence comes into play with repeat-pass InSAR collections, like those used in this report. An equation for temporal coherence assuming random motion of the scatterers between passes is given as [6]

$$\gamma_t = exp\left\{ -\frac{1}{2}\left(\frac{4\pi}{\lambda}\right)^2 \left[\sigma_y^2 \, sin^2\theta \; + \; \sigma_z^2 \, sin^2\Theta \right]\right\} \tag{3}$$

and

Θ is the look angle to the scattering cell,

λ is the wavelength at the center frequency,

θ is the angle of arrival of the return signal,

σ_y is the root mean square (RMS) motion of the scatterer in the cross-track direction,

σ_x is the root mean square (RMS) motion of the scatterer in the elevation direction.

The coherence as a function of signal-to-noise (SNR) was shown to be [6]

$$\gamma_{snr} = \frac{1}{1 + SNR^{-1}} \, . \tag{4}$$

Equation 4 shows that the coherence will be reduced with more noise in the RADAR system.

The coherence relies on the registration of two images. If there are errors in this registration, the coherence will decrease. For a rectangular impulse response, the coherence function will be a sinc function [7], and a sinc impulse response will produce a triangle function [6]. Therefore, the inaccuracy of registration falls off as a function of the position error.

The geometric coherence places a limit on the maximum observation angle difference possible while retaining coherence. This angular limit can be defined in terms of the distance between antenna aperture centers for the interferometric pair. The distance between antenna aperture centers at the center of each aperture is called the baseline. The baseline distance at which the pair has no coherence is called the critical baseline. The coherence as a function of geometry can be expressed in terms of the geometry and spatial resolution of the collects in range [8] as

$$|\gamma_{g,r}| = \left| sinc\left[\frac{2\pi}{\lambda}\rho_r tan(\phi + \alpha)\Delta\phi\right]\right| \quad (5)$$

where

ρ_r is the spatial resolution in range,

ϕ is the depression angle to the target scene center,

α is the local slope of the terrain over the resolution cell,

$\Delta\phi$ is the angle separating the antennas relative to the clutter cell.

For the cross-range, the azimuth direction, the geometrical coherence is

$$|\gamma_{g,az}| = \left| sinc\left[\frac{2\pi}{\lambda}\rho_a\Delta\phi\right]\right| \quad (6)$$

where

ρ_a is the spatial resolution in azimuth,

$\Delta\phi$ is the angle separating the antennas relative the resolution cell.

The estimation of the total coherence is given by

$$|\gamma| = \frac{\left|\sum_{i=1}^{N}\sum_{j=1}^{N} g_{ij}^{*} h_{ij}\right|}{\left|\sum_{i=1}^{N}\sum_{j=1}^{N} |g_{ij}|^2 \sum_{i=1}^{N}\sum_{j=1}^{N} |h_{ij}|^2\right|}. \quad (7)$$

where

g_{ij} is the master complex-valued image at i, j in range and azimuth,

h_{ij} is the registered slave complex-valued image at i, j in range and azimuth,

N is window size in range and azimuth designating an estimation box. This window does not have to be symmetrical.

While equation 7 gives the magnitude, the numerator without the absolute value gives a magnitude and phase difference between the two complex images. Given a broad-side geometry like that in Figure 2-1,

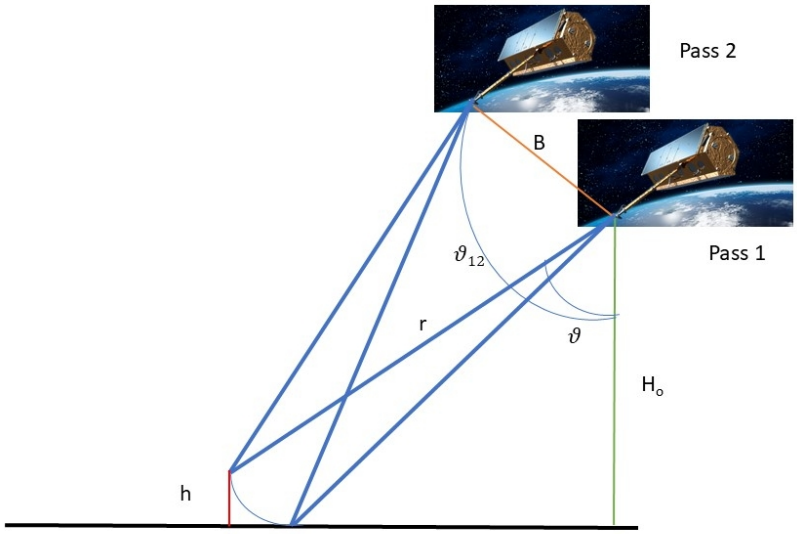

Figure 2-1: Geometry of two-pass SAR interferometry.

the phase difference is given by

$$\Delta\Phi = \frac{4\pi(|\vec{B}|\cos(\vartheta - \vartheta_{12}))}{\lambda} \quad , \tag{8}$$

where B is the baseline, and ϑ is the look angle for repeat pass collections [1] [9] [10]. The height is found by

$$\vartheta = \vartheta_{12} - cos^{-1}\left(\frac{\Delta\Phi\lambda}{4\pi|\vec{B}|}\right) \tag{9}$$

$$h = H - rcos\vartheta. \tag{10}$$

Finding the height at every resolved image pixel will then produce a digital elevation model (DEM). Notice, however, that equation 7 specifies the coherence and phase are spatial estimations, so the DEM will have coarser resolution than the original SAR images. Sandia's approach to InSAR can be found in [11].

Figure 2-2 shows an example of the phase difference, also called an interferogram, over Rock Valley produced by images 4 and 5 in radar coordinates. Range is up and down, cross-range is left to right. Figure 2-2 shows that the phase difference is modulo 2π. Therefore, the phase difference must be unwrapped to calculate the height. We use the Goldstein method to unwrap the phase difference [8].

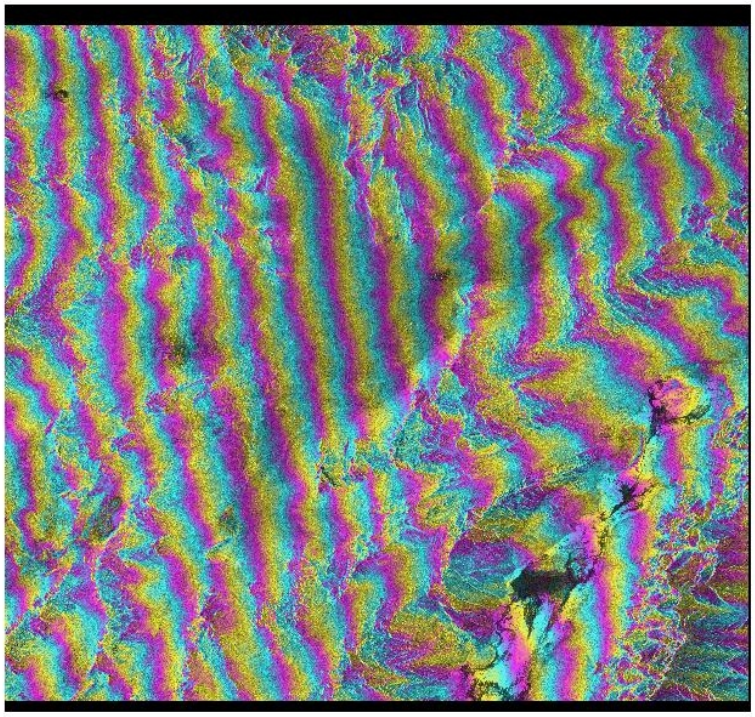

Figure 2-2: Phase difference using images 4 and 5 from Table 2-1 in radar coordinates. Near range is the right edge of the image. Far range is the left edge of the image. Cross range is up and down on the image. The phase difference is modulo 2π .

The phase difference is dependent on the coherence. In fact, the phase difference fringes are crisp and well-defined with high coherence and noisy, ill-defined, and even non-existent with low coherence. This relationship between the fringes and coherence is known as fringe visibility [12]. Fringes become noisy within low coherent areas and can be hard to unwrap. Figure 2-3 shows the estimated coherence in radar coordinates for the interferometric pairs used to produce Figure 2-2.

In Figure 2-3, white is high coherence, thus good fringe visibility is possible. Black is low coherence, which includes shadows, water, and perhaps steep terrain. Previous SPE research has shown that low coherence can also be due to surface change [13]. Coherence change may show rock movement or landslides.

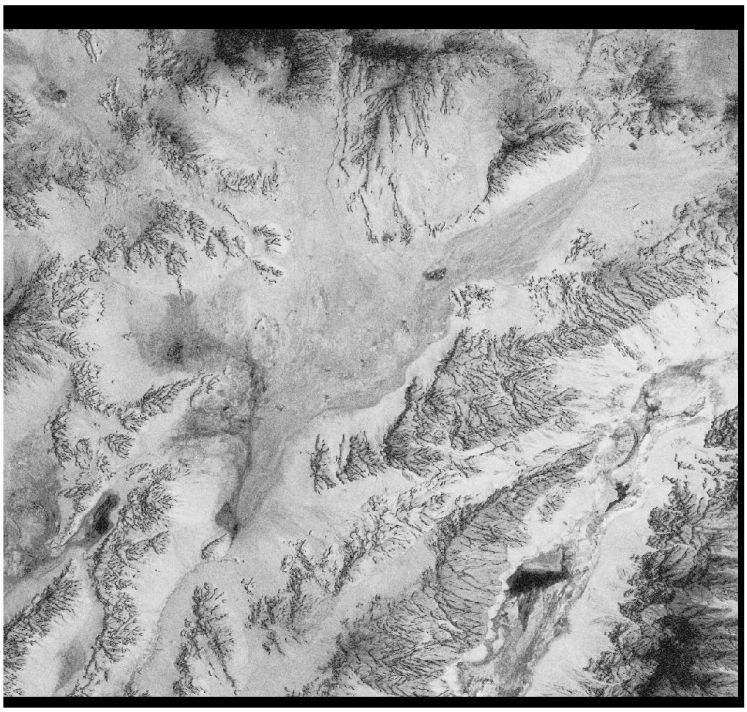

Figure 2-3: Coherence of images 4 and 5 in radar coordinates. Near range is the right edge of the image. Far range is the left edge of the image. Cross range is up and down. White is high coherence. Black is low coherence or no data. Shadows and water have low coherence.

2.2. SAR Differential Interferometry

With robust registration and good repeat-pass geometry, $|\gamma_s| \approx 1$ so that $|\gamma| \approx |\gamma_t| \cdot |\gamma_{snr}|$. Designing the collection and radar so that SNR is high and there is low temporal change, phase difference fringes will capture topography. These phase difference fringes will be identical if more than one interferometric pair are collected from the same geometry. However, if height change occurs and the temporal coherence is preserved, equation 3, the change in phase will not be the static topography, but rather, a change in height between collection given by

$$\Delta\phi_{12} = \frac{4\pi \mathrm{B}_{12}\cos(\vartheta)}{\lambda} \quad \text{and} \tag{11}$$

$$\Delta\phi_{23} = \frac{4\pi \mathrm{B}_{13}\cos(\vartheta + \alpha)}{\lambda} \tag{12}$$

where ϑ is the angle between phase centers and boresight for passes 1 and 2, and $\vartheta + \alpha$ describes the angle between phase centers and boresight for passes 2 and 3 [1]. If the apertures are closely matched, the difference of the phase difference is

$$\delta(\Delta\phi) = \frac{4\pi}{\lambda}\Delta r \tag{13}$$

where Δr is the range change that occurred after pass 2 and before pass 3.

This approach can be viewed as if pass 1 and 2 interferogram creates a current DEM. And passes 2 and 3 measure if that DEM has changed over the time lapse between pass 2 and pass 3. Therefore, if

an accurate DEM exists, the DEM and the collection geometry can be used to create an ideal phase difference fringe map, and this ideal phase difference, can be compared to any interferometric pair to monitor change.

2.3. SAR Differential Interferometry and Earthquakes

The change phase difference given in equation 13 has been used to show the surface deformation from earthquakes. Figure 2-4 shows the differential phase difference produced by the October 16, 1999 7.1 Mw Hector Mine earthquake which is the southmost differential phase difference. This fringe map was generated using ERS-1 September 9, 1999 and October 20, 1999 interferometric pairs [14]. Figure 2-4 also shows the differential phase difference produced by the Rock Valley earthquake series which is the northmost differential phase difference. This fringe map was generated using image 5 and image 7 in Table 2-1. The differential interferometric processing used the same processing chain for both data sets. The Rock Valley interferometric pair of image 5 and image 7 span the time from March 3, 1993 to June 18, 1993. Table 2-2 shows the seismic events recorded during that time span that point to activity in Rock Valley.

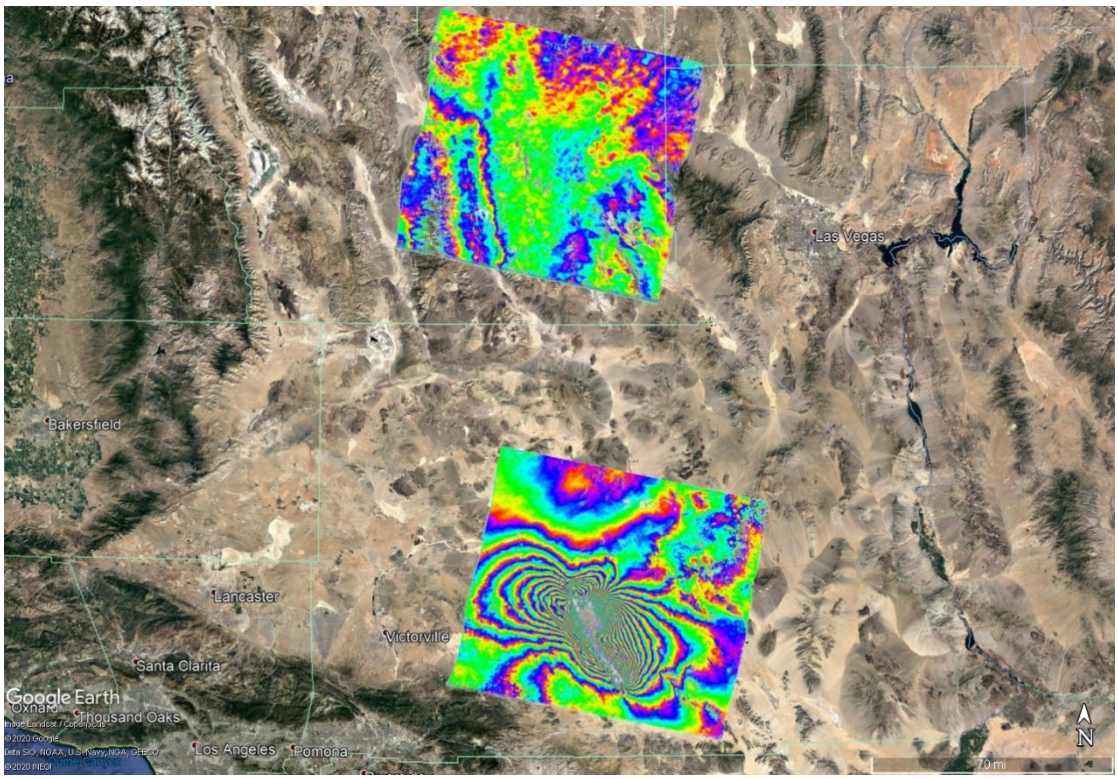

Figure 2-4: Differential InSAR fringes between March 3, 1993 and June 18, 1993 (top) encompassing a portion of the Rock Valley earthquake series, and between September 9, 1999 and October 20, 1999 (bottom) encompassing the 1999 7.1 Mw Hector Mine Earthquake.

Table 2-2: Rock Valley seismic events [15]

Event	Date/Time	Latitude (°N)	Longitude (°W)	Mw
1	05/30/93, 1520	36:43.11	116:06.95	3.7
2	05/31/93 0315	36:43.23	116:07.17	2.4
3	05/31/93 0918	36:42.98	116:07.86	2.6
4	05/31/93 1113	36:43.41	116:06.66	2.1
5	05/31/93 1244	36:43.32	116:06:78	2.9
6	05/31/93 2238	36:43.32	116:07.09	2.0
7	06/01/93 1628	36:43.21	116:06.95	2.8
8	06/03/93 0835	36:43.37	116:06.51	2.2
9	06/03/93 1720	36:42.96	116:07:49	2.4
10	06/04/93 1623	36:43.22	116:08.18	2.0
11	06/05/93 1323	36:42.89	116:07.67	2.5
12	06/06/93 1531	36:43.22	116:06.93	2.5

One additional step that was used but not discussed above, was removal of orbital induced fringes from both data sets. This is done by selecting a ground control point in the scene where the terrain is relatively flat [16]. Even with this correction, there is some residual terrain (low frequency) in both differential interferograms in Figure 2-4.

In Figure 2-4, the Hector Mine differential interferogram shows high frequency phase fringes. The Rock Valley differential interferogram does not exhibit high-frequency fringes. Tightly spaced fringes mean large displacement occurred according to equation 13. Since SAR measures range, the range difference from equation 13 can be separated into horizontal and vertical displacement. Given just these results in Figure 2-4, we can conclude no large-scale earth movement occurred for the Rock Valley earthquake series. However, we cannot conclude there was no earth movement. Therefore, we need to dig deeper.

3. DIGGING DEEPER

In this section, we explore subtle earth movement measurements by comparing differential SAR results in Rock Valley as a function of time. We also explore if the SAR coherence between InSAR pairs provides any clues as to surface changes, and if so, where these surface changes might have occurred. Finally, we look at other algorithms that can refine the differential height measurements and we explore if they can be used to confidently detect small earth movement.

3.1. A Time Series of Differential InSAR

Given the InSAR pairs in Table 2-1, we can construct three differential InSAR (DInSAR) pairs that will create a time series spanning January 29, 1993 to July 23, 1993. Using the processing chain presented above, DInSAR from January 29 to March 5, 1993, March 5, 1993 to June 18, 1993, and June 18, 1993 to July 23, 1993 are produced.

Figure 3-1 shows a geolocated zoomed product of differential height displacements. Rock Valley is in the center, where the line transects the valley. Along this transect, which is approximately 40.5 km long, displacement measures were taken. These are shown in the plots in Figure 3-1. As discussed above, the noise level for the ERS-1 differential height measures are 3 mm, therefore height displacements greater than 5 mm are reasonable to examine being high enough above the noise floor.

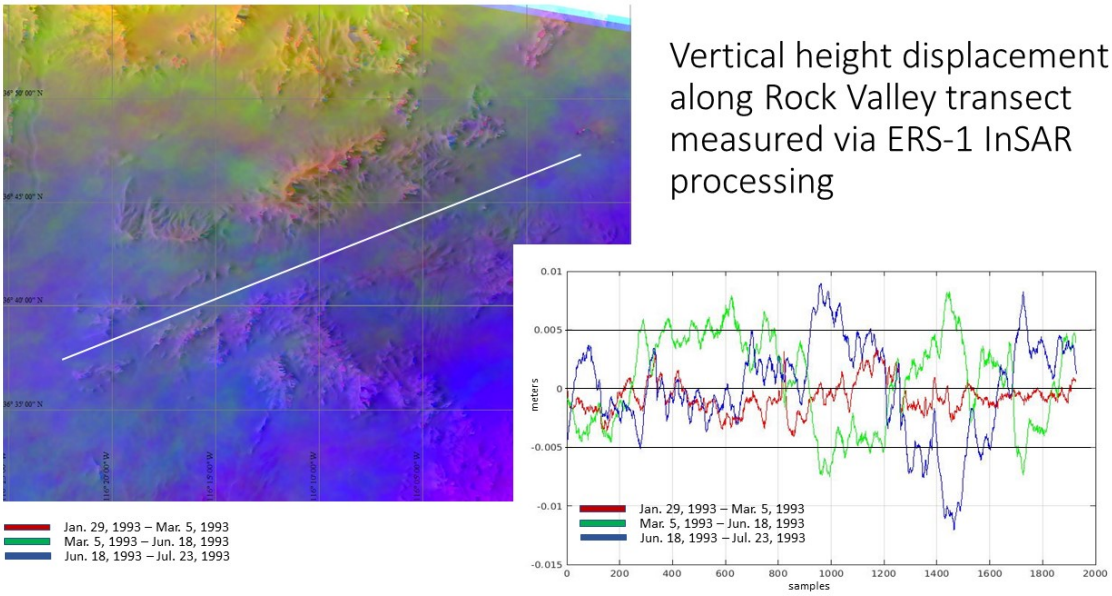

Figure 3-1: Time series differential InSAR. The color image is created using Red, Green, and Blue channels. The Red channel is January 29 – March 5, 1993 vertical displacement. The Green channel is the March 5 – June 18, 1993 vertical displacement, and the Blue channel is the June 18 – July 23, 1993 vertical displacement. The displacement profiles along the white line (the transect) are shown in the graph.

Note in Figure 3-1 the red plot, which is January 29 – March 5, 1993 has no remarkable movement. March 5 – June 18, 1993 has some motion larger than 5 mm, and June 18 – July 23, 1993 also shows some displacements larger than 5 mm.

The March 5 – June 18, 1993 height displacement transect is shown by itself in Figure 3-2 to highlight where subtle surface motion occurs with respect to the largest earthquake event which is marked as a star. Red circles are areas of apparent uplift. The yellow circles show areas of apparent subsidence. Note that these do not coincide with the event location as denoted by the star on the image.

In a similar manner, the June 18 – July 23, 1993 height displacement transect is shown by itself in Figure 3-3 to highlight where subtle surface motion occurs with respect to the largest earthquake event marked as a star. Red circles are areas of apparent uplift. The yellow circles show areas of apparent subsidence. Note that these do not coincide with the precise earthquake location.

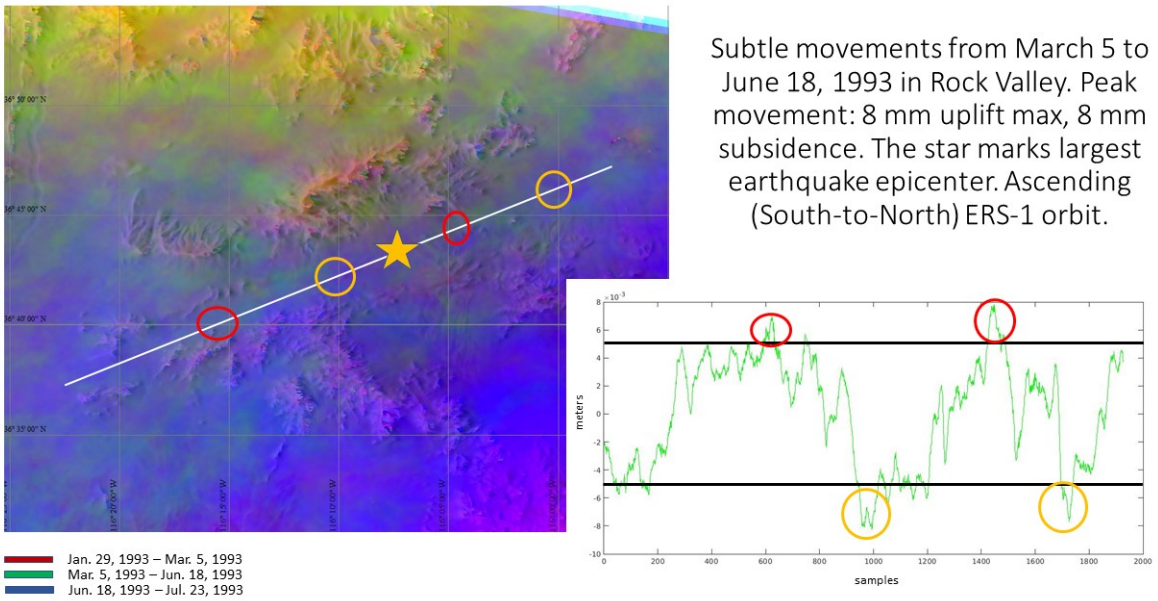

Figure 3-2: March 5 – June 18, 1993 differential InSAR height displacement. Red circles mark apparent uplift and yellow circles mark apparent subsidence. Changes do not coincide exactly with the largest earthquake event location – the star on the transect.

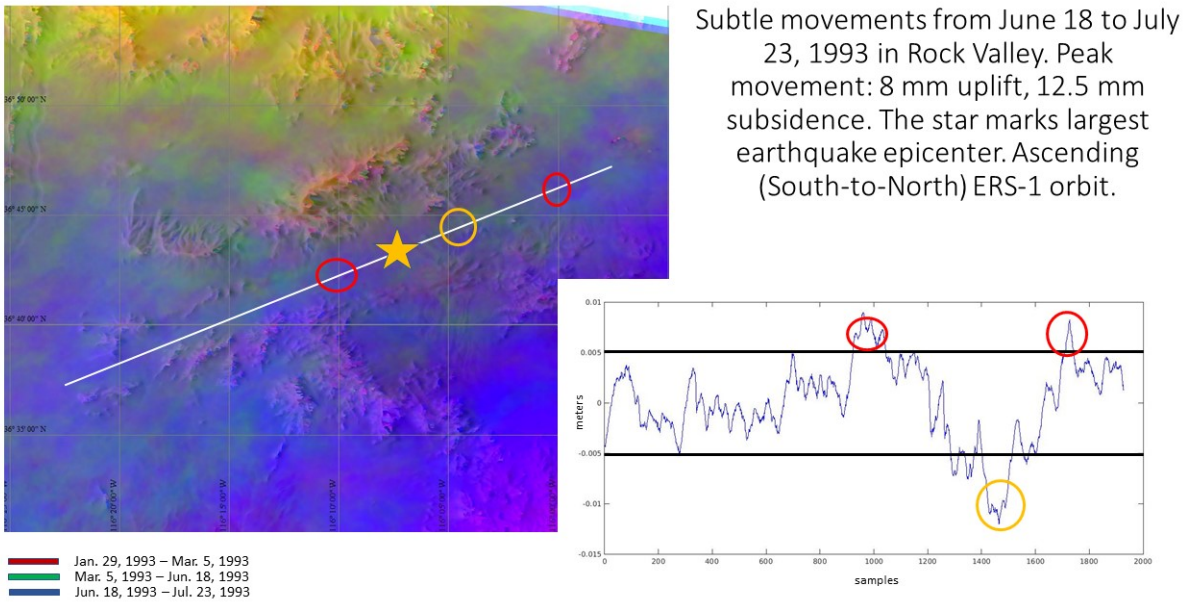

Figure 3-3: June 18 – July 23, 1993 differential InSAR height displacement measurements. Red circles mark apparent uplift and the yellow circle marks an apparent subsidence. The star on the transect denotes the largest earthquake event.

Examining the plots from Figure 3-2 and Figure 3-3, note that the Figure 3-2 (March to June) surface subsidence spatial position closely coincides with the Figure 3-3 (June to July) uplift position. Also, the eastern-most uplift from Figure 3-2 (March to June) has a subsidence event in Figure 3-3 (June to July). The western-most uplift in Figure 3-2 does not have an opposite direction movement in Figure 3-3. The subsidence in Figure 3-2 and the uplift in Figure 3-3 are almost the same values so the final vertical displacements are less than 5 mm.

Until now, the vertical displacement has been attributed to the earthquake. Could something else lead to this apparent change? The answer is yes. While SAR is advertised as a day and night, all-weather sensor, when the phase or phase difference is exploited, the atmospheric content can cause delays, and thus, phase differences between collections. Remember that the Rock Valley location is dry and arid, but even the desert gets clouds and rain sometimes. Atmospheric removal needs to be explored, but first, the coherence is readily available to examine.

3.2. A Time Series of SAR Coherence

The SAR coherence, using equation 7, was estimated for the InSAR pair of images 4 and 5, InSAR pair of images 5 and 7, and InSAR pair of images 7 and 8. A red-green-blue (RGB) composite of the coherences is shown in Figure 3-4.

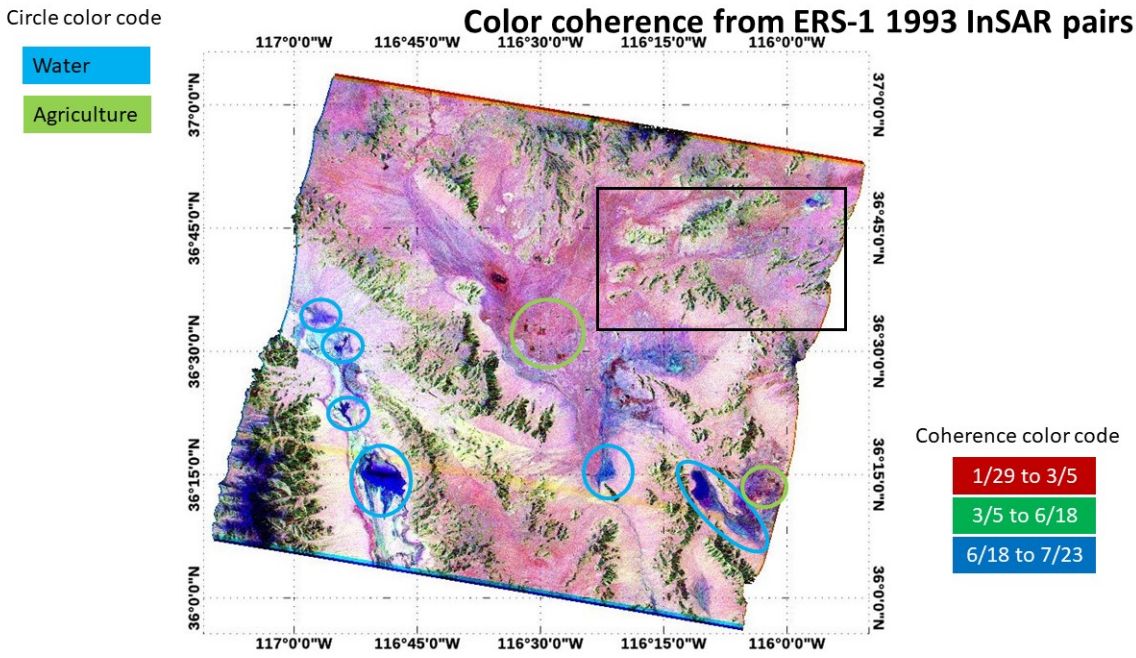

Figure 3-4: Geolocated color composite of the coherence for the entire ERS-1 footprint spanning the dates of January 29, 1993 to July 23, 1993. This footprint encompasses Rock Valley. Legend gives bands corresponding to coherence dates. Also, agriculture is circled in green. Water drainage features are circled in blue. The black rectangle shows the area that is shown in Figure 3-6.

If the ERS-1 coherence was constant over the period from January to July 1993, Figure 3-4 would possess gradations of gray as coherence similar to the coherence in Figure 2-3. Since Figure 3-4 has colors, the coherence has changed differently for each period captured by the RGB bands. The pinkish hue is from the January to March coherence being the highest value. Whitish colors on mountain sides shows the coherence is almost constant there. Blue color means that the red (January to March coherence) and the green (March to June coherence) is low. The appearance of the blue features suggests water drainage and water accumulation. Coherence drops when the earth is wet, or for water. The water may be gone during the June to July coherence, producing a better coherence during this period. Parts of the ERS-1 footprint denote agriculture because the coherence is constantly low but not absent in a flat region. This is confirmed with satellite imagery from Google Earth© in Figure 3-5. The green circles in Figure 3-5 are the same areas as denoted by green circles in Figure 3-4. The circular vegetation are agriculture fields.

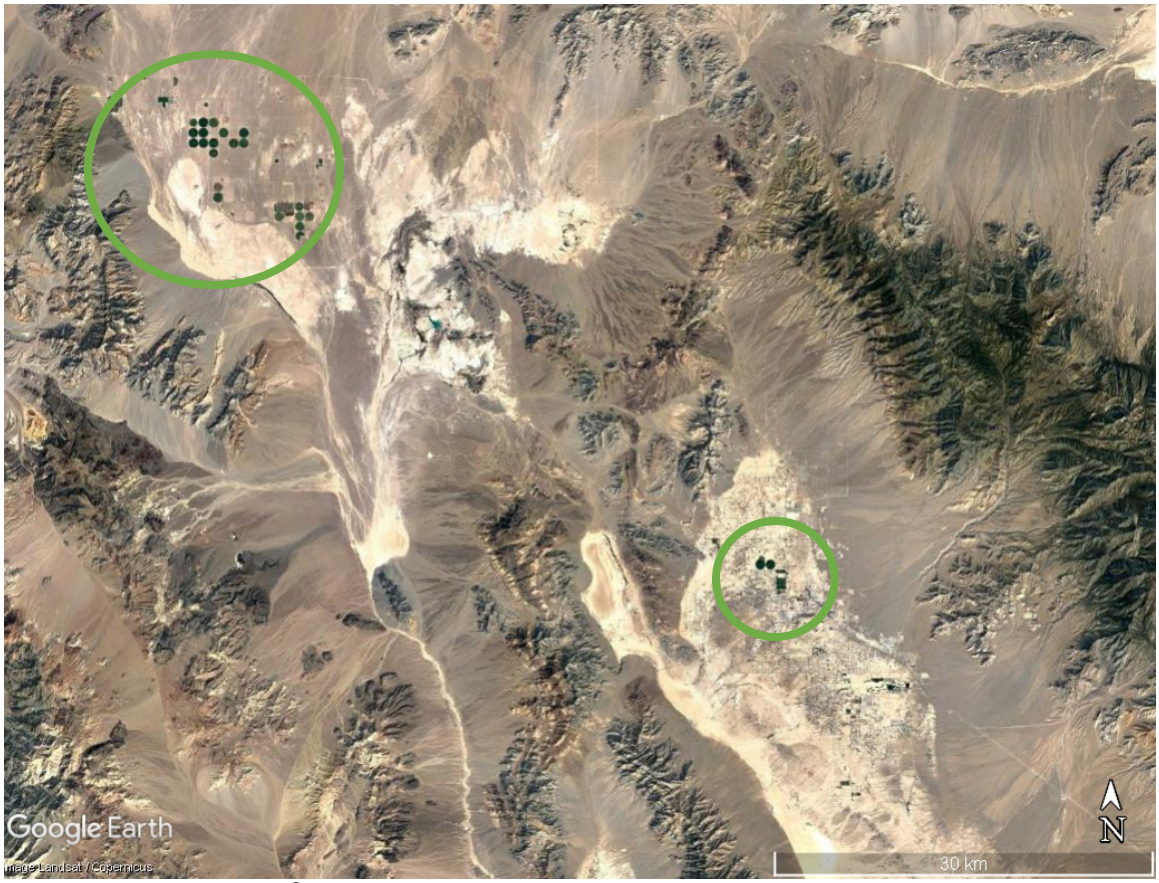

Figure 3-5: Google Earth© image of a portion of the ERS-1 footprint. There are some agriculture fields that lead to coherence drop in Error! Reference source not found..

Figure 3-6**Error! Reference source not found.** shows the color composite coherence zoomed in on the Rock Valley area. Dark areas are shadows from the mountains where there is no signal, thus no coherence can be estimated. Note that most of the mountain sides are whitish or light pink showing the coherence over those targets is relatively unchanged. Red hues indicate the January to March was the most coherent pair. The yellow circles draw attention to areas with coherence decrease. The coherence here has red and bluish tints, meaning that the coherence in the period of the earthquake activity is lower, otherwise green hue would also be present. This decrease in the March to June coherence could be due to the earthquake activity. Yet, coherence change due to moisture change cannot be ruled out, even though this area is desert. Note the drainage feature's coherence change in the upper right corner of the coherence map. The drop in coherence is not unique to surface change caused by an earthquake. A drop in coherence can occur because of changes caused by water drainage, and standing water, also.

Figure 3-7 shows an optical image of Rock Valley with the area of low coherence denoted by a yellow trapezoid. The coherence drop is over an approximate 13 square km area south southeast of Skull Mountain centered at 36° 43' 30" N latitude and 116° 05' 00" W longitude as outlined by the yellow trapezoid in the figure. This center location is close in latitude to many of the earthquake event locations in Table 2-2, but is slightly east of where the seismic events apparently occurred. The low-coherence area extends from approximately 116° 07' 00" W longitude to 116° 03' 30" W longitude.

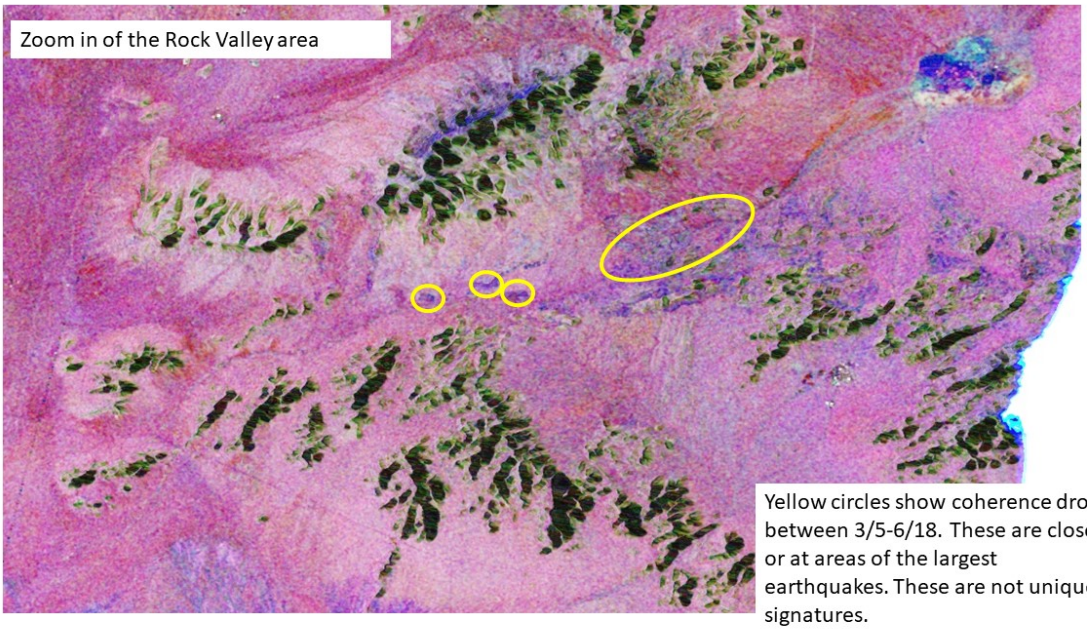

Figure 3-6: Zoomed Rock Valley portion of the ERS-1 color composite coherence in Figure 3-4. Note the drainage feature in the upper right (looks bluish and purple). Also, note the drop in coherence along the Rock Valley ground denoted by the yellow circles.

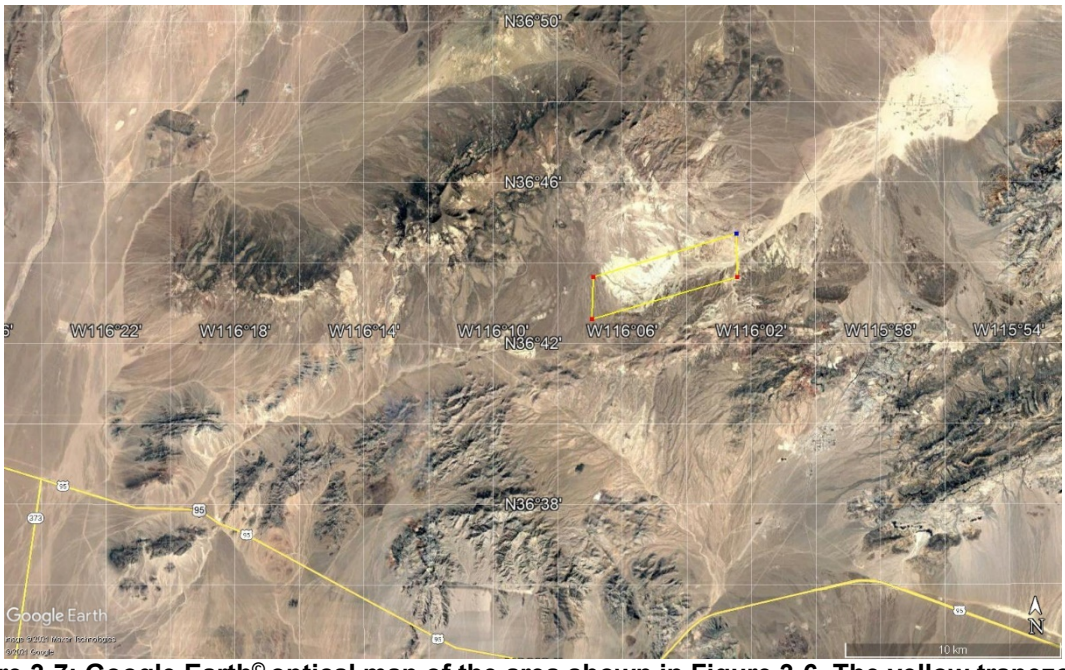

Figure 3-7: Google Earth© optical map of the area shown in Figure 3-6. The yellow trapezoid is largest area of coherence drop shown in Figure 3-6. The smaller yellow circles are very near the road (Jackass Flats Road) that cuts through this portion of NNSS.

3.3. Summary of Time Series Findings

Differential InSAR results from ERS-1 through 1993 over Rock Valley show no height displacement change from January to March 1993. From March to June 1993, small height displacements with a maximum of 8 mm uplift and a maximum of 8 mm subsidence are measured along a 40 km transect through Rock Valley. From June to July 1993, uplifts of 9 mm coincided at the areas of the 8 mm subsidence from March to June 1993, and one area of 12 mm subsidence coincided with an area of 8 mm uplift from March to June 1993. One area of uplift, the southwest most uplift displacement of 8 mm, did not have an opposite surface movement during June to July 1993. Therefore, a resulting 8 mm or 0.315-inch displacement was measured.

Coherence measures over the same three time periods show there was water drainage activity over the desert. Coherence over the Rock Valley transect dropped over the area of the earthquake activity from March to July 1993. This decrease in coherence may be due to the earthquakes, but water drainage cannot be ruled out, since the area is a valley and a large water drainage disturbance is apparent at the northwest end of the valley.

In a forensic-like manner, we explored the possibility of earthquake induced earth displacement. A tangible displacement is found, but there is one component of error in the measurement that has not been eliminated. As presented in Section 3.1, atmospheric delay difference over time can induce differential phase that could be interpreted as height changes. Even though Rock Valley is desert, atmospheric delays in the data must be explored.

3.4. Other Differential InSAR Approaches

Section 3.1 shows how a time series of DInSAR products can be used to find subtle changes in the earth surface movement. What if the time series can be extended to many interferometric pairs that spans more time? Other DInSAR approaches used this framework as is presented below.

3.4.1. Persistent Scatters

A differential InSAR technique has been developed for long-term subsidence monitoring, where there might be time gaps between coherent InSAR pairs. If a multi-temporal set is available, coherent point targets can be used to monitor their motion. This is called persistent scatterers method and is very useful in urban areas [17].

Permanent scatters in nonurban areas may be very sparse and hard to select. This is the case with Rock Valley. Most of the reflectors there are diffuse reflectors.

3.4.2. Small Baseline Subset (SBAS)

Another InSAR approach is the small baseline subset (SBAS) technique. SBAS relies on a combination of differential interferograms created by small orbital baselines [18]. For ERS-1, the available acquisitions are generally distributed in several small baseline subsets separated by large baselines. The singular value decomposition (SVD) technique is used to link the small baseline subsets, increasing the temporal sampling rate. Atmospheric artifacts are filtered out based on both spatial and temporal information. The static topographic phase is removed using the phase difference simulated using a DEM.

The SBAS technique creates interferograms having mutual small baselines given a collection of coherent SAR images such as those in Table 2-1. For our area, we did not find InSAR pairs before

April 1992 or after November 1993. With respect to the SBAS approach, this is a limited data set. Most data sets span two or more years with 15 or more coherent images.

The computed differential interferograms are organized into a linear model given by

$$B\boldsymbol{v} = \delta\boldsymbol{\phi}, \tag{14}$$

where B is a matrix defining the small baseline combinations, $\delta\boldsymbol{\phi}$ is the vector of unwrapped differential interferometric phase values, and $\boldsymbol{v}$ is the vector of unknown mean phase velocities associated with any deformation.

A minimum-norm least squares solution of equation 14 is obtained by using the SVD method

$$\boldsymbol{v} = V\begin{bmatrix}\Sigma^{-1} & 0\\ 0 & 0\end{bmatrix}U^T\delta\boldsymbol{\phi}\ , \tag{15}$$

where V, U, and Σ^{-1}= diag(σ_1^{-1},. . .,$\sigma_{N\text{-}L+1}^{-1}$) are the SVD decomposition of B, N is the number of images, and L is the number of subsets. U^T denotes the transpose of U.

The atmospheric artifacts are estimated and removed based on the space-time information available. If the model from equation 14 is valid, phase residues are due to atmospheric effects different than a phase ramp and phase noise [18]. The atmospheric components can be removed by smoothing spatially the phase residues relative to the master image phase.

3.4.3. SBAS for Rock Valley

Originally, the SBAS approach was attempted with images 4 through 11 in Table 2-1. These images were known to be coherent pairs. However, the SVD method was ill-conditioned, and results could not be solved. Subsequently, images 1 to 3 in Table 2-1 were discovered and added to the SBAS process. With these additional images, only the December 1992 (image 3) contributed to the SBAS process.

The SBAS process was performed on our data set using software called SARScape by L3-Harris. With the nine images from image 3 to image 12, the algorithm fits a linear model to the differential phase. The SVD inversion was accomplished, but the number of images was suboptimal. The resulting total displacement from December 1992 to November 1993 is shown in Figure 3-8.

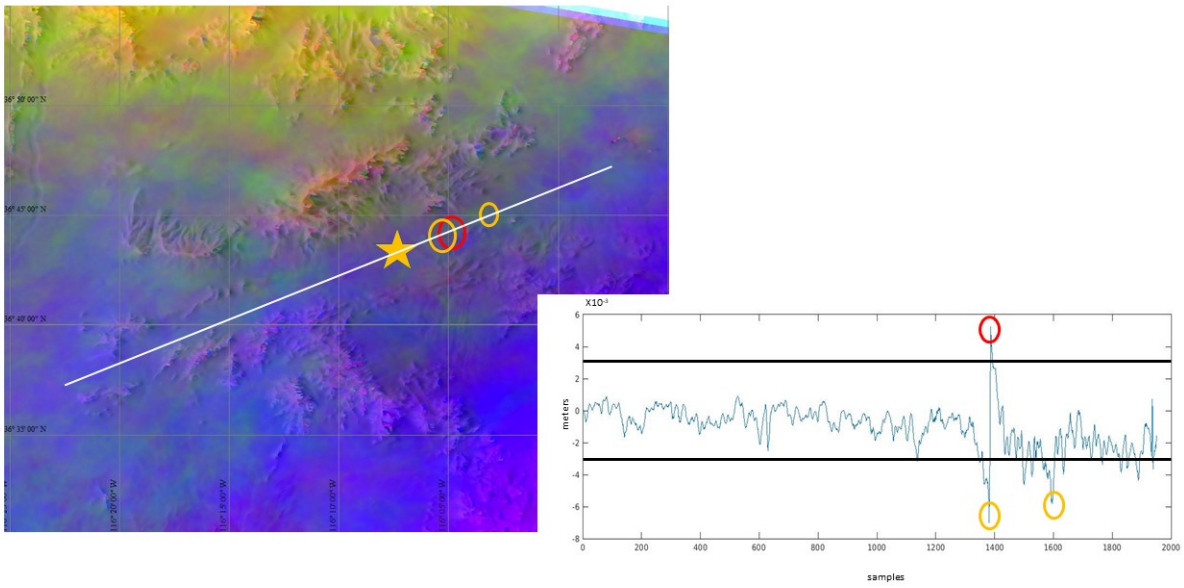

Figure 3-8: SBAS overall displacement from December 1992 to November 1993 over the same Rock Valley transect of approximately 40 km. The displacement is localized just northwest of the strongest seismic measures.

The Figure 3-8 transect plot includes atmospheric corrections. Here the 5 mm displacement threshold was decreased to 3 mm since atmospheric phase has been systematically removed. The displacement results are minimal except for a "large" event that has a total magnitude of ~13 mm or 0.51 inches. This subsidence and uplift jump could be a phase discontinuity called a jump cycle, where the interferogram phase unwrapping is not smooth and a 2π ambiguity is not resolved. Inspection of all the interferograms reveals that the December 1992 to January 1993 has what appears to be a phase jump cycle in the Rock Valley area.

If the phase ambiguity is removed, the displacement is shown in Figure 3-9. Again, the 5 mm displacement threshold was decreased to 3 mm since atmospheric phase has been systematically removed. As suggested in Section 3.1, the difference of the transect data is almost no movement overall. This is demonstrated with the SBAS processing. Given the subtle change these results imply, the results are not definitive. Considering all the assumptions and processing, displacements this small are difficult to verify. In fact, without ground truth, this change cannot be verified.

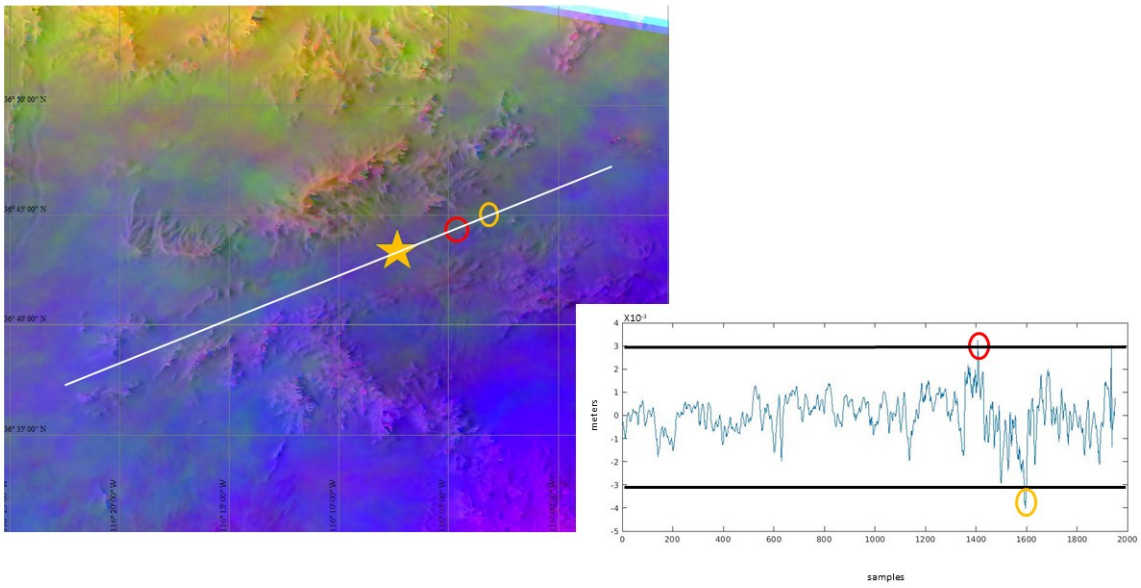

Figure 3-9: SBAS displacement results with the jump cycle removed. A slight uplift and subsidence may have occurred over the one-year time span.

4. CONCLUSION

We have shown two approaches to determine surface height displacement from ERS-1 legacy InSAR imagery data. Examining imagery from 30 years ago can be likened to a forensic review of surface changes.

While small earthquakes did occur during 1993 centered near Rock Valley, Nevada, other acts of nature may have also occurred during this time frame. One relevant natural act is erosion. Movement of soils in the valley due to water or high winds could cause surface height changes.

We found no major height changes in Rock Valley during 1993. However, we did find subtle height changes – subtle being 12 mm (0.5 inches) or less in isolated locations. These subtle height changes could have been from differing atmospheric delays between the days of the SAR collections. Yet, with atmospherics removed from the data using the SBAS process, height changes were still discovered near the seismically-active area.

An InSAR coherence drop occurred in an area south southeast of Skull Mountain centered at 36° 43' 30" N latitude and 116° 05' 00" W longitude. DInSAR measured subtle height changes here also.

Even though there are surface changes in height and reduction in SAR coherence, these changes cannot be solely linked to earthquake activity. Rain, water drainage, and water and wind erosion can also play a role in such changes. Therefore, using ERS-1 InSAR processing to detect earthquake activity in Rock Valley, Nevada during 1993 is inconclusive. This result is not surprising, for from a literature search, the smallest earthquake magnitude previously detected by InSAR techniques that we could find was the 2008 Reno-Mogul 4.7 Mw earthquake swarm. The displacement there was 2.5 cm and it affected an area of 150 km^2 [5].

Nevertheless, a process of creating products to calculate differential height measures as well as coherence measures in a forensic-like exploration of data is shown to have merit. Without ground-truth, the subtle height change results found with this ERS-1 data set over Rock Valley, NV cannot be confirmed to be products of the earthquake activity. However, future experiments at Rock Valley can be monitored by satellite InSAR collects and compared to ground truth, providing another dimension to earthquake/explosion monitoring.

REFERENCES

[1] A. K. Gabriel, R. M. Goldstein and H. A. Zebker, "Mapping small elevation changes over large areas: Differential interferometry," *Journal of Geophysical Research,* pp. 9183-9191, July 1989.

[2] D. Massonnet, M. Rossi, C. Carmona, F. Ardagna, G. Peltzer, K. Feigl and T. Rabaute, "The displacement field of the Landers earthquake mapped by radar interferometry," *Nature,* pp. 138-142, July 1993.

[3] G. Peltzer and P. A. Rosen, "Surface displacement of the 17 May 1993 Eureka Valley, California, earthquake observed by SAR interferometry," *Science,* pp. 1333-1336, June 1995.

[4] S. Stramondo, M. Tesauro, P. Briole, E. Sanossti, S. Salvi, R. Lanari, M. Anzidei, P. Baldi, G. Fornaro, A. Avallone, F. Buongiorno, G. Franceschetti and E. Boschi, "The September 26, 1997 Colfiorito, Italy earthquakes: Modeled coseismic surface displacement from SAR interferometry and GPS," *Geophyical Research Letters,* pp. 883-886, April 1999.

[5] J. W. Bell, A. F. and C. D. Henry, "InSAR analysis of the 2008 Reno-Mogul earthquake swarm: Evidence for westward migration of Walker Lane sytle dextral faulting," *Geophysical Research Letters,* vol. 39, p. L18306, 26 September 2012.

[6] H. A. Zebker and J. Villasenor, "Decorrelation in interferometric radar echos," *IEEE Transactions on Geoscience and Remote Sensing,* pp. 950-959, September 1992.

[7] R. Bamler and D. Just, "Phase statistics of interferograms with apllications to synthetic aperture radar," *Applied Optics,* pp. 4361-4368, July 1994.

[8] R. M. Goldstein, H. A. Zebker and C. L. Werner, "Satellite radar interferometry: two-dimensional phase unwrapping," *Radio Science,* pp. 713-720, July 1988.

[9] F. K. Li and R. M. Goldstein, "Studies of Multibaseline spaceborne interferometric synthetic aperture radars," *IEEE Transactions on Geoscience and Remote Sensing,* vol. 28, no. 1, pp. 88-97, 1990.

[10] S. N. Madsen, H. A. Zebker and J. and Martin, "Topographic mapping using radar interferometry: processing techniques," *IEEE Transactions on Geoscience and Remote Sensing,* vol. 31, no. 1, pp. 246-256, 1993.

[11] D. L. Bickel and W. H. Hensley, "Design, Theory, and Application of Interferometric Synthetic Aperture Radar for Topographic Mapping," Sandia National Labs - SAND96-1092, Albuquerque, 1996.

[12] M. Born and E. Wolf, Principles of Optics, New York: Pergamon Press, 1980.

[13] D. A. Yocky, R. D. West, R. M. Riley and T. M. Calloway, "Monitoring surface phenomena created by an underground chemical explosion using fully polarimetric VideoSAR," *IEEE Transactions on Geoscience and Remote Sensing,* vol. 57, no. 5, pp. 2481-2493, 2019.

[14] M. Simons, Y. Fialko and L. Rivera, "Coseismic deformation from the 1999 Mw 7.1 Hector Mine, California, earthquake as inferred from InSAR and GPS observations," *Bulletin of Seismological Society of America,* vol. 92, no. 4, pp. 1390-1402, 2002.

[15] K. D. Smith, J. N. Brune and G. Shields, "A sequence of very shallow earthquakes in the Rock Valley fault zone, southern Nevada Test Site," U.S. Geological Open File Report - Seismic Hazard Issues Yucca Mountain, 2000.

[16] D. Massonnet and K. L. Feigl, "Radar interferometry and its application to changes in the earth's surface," *Reviews of Geophysics,* vol. 36, no. 4, pp. 441-500, 1998.

[17] A. Ferretti, C. Prati and F. Rocca, "Permanent scatterers in SAR interferometry," *IEEE Transactions on Geoscience and Remote Sensing,* vol. 39, no. 1, pp. 8-20, 2001.

[18] P. Berandino, G. Fornaro, R. Lanari and E. Sansosti, "A new algorithm for surface deformation monitoring based on small baseline differential interferograms," *IEEE Transactions on Geoscience and Remote Sensing,* vol. 40, no. 11, pp. 2375-2383, 2002.

DISTRIBUTION

Email—Internal

Name	Org.	Sandia Email Address
Robert Abbott	8911	reabbot@sandia.gov
Steven Castillo	5340	spcasti@sandia.gov
Mark Diltz	5346	madiltz@sandia.gov
Stephanie Teich-McGoldrick	6756	steichm@sandia.gov
David Yocky	5346	dayocky@sandia.gov
Technical Library	01977	sanddocs@sandia.gov

This page left blank

This page left blank

Sandia National Laboratories

Sandia National Laboratories is a multimission laboratory managed and operated by National Technology & Engineering Solutions of Sandia LLC, a wholly owned subsidiary of Honeywell International Inc. for the U.S. Department of Energy's National Nuclear Security Administration under contract DE-NA0003525.